Coherent Control of Nanoscale Ballistic Currents in Transition Metal Dichalcogenide ReS_2

Qiannan Cui and Hui Zhao*

Department of Physics and Astronomy, The University of Kansas, Lawrence, Kansas 66045, United States

ABSTRACT Transition metal dichalcogenides are predicted to outperform traditional semiconductors in ballistic devices with nanoscale channel lengths. So far, experimental studies on charge transport in transition metal dichalcogenides are limited to the diffusive regime. Here we show, using ReS_2 as an example, all-optical injection, detection, and coherent control of ballistic currents. By utilizing quantum interference between one-photon and two-photon interband transition pathways, ballistic currents are injected in ReS_2 thin film samples by a pair of femtosecond laser pulses. We find that the current decays on an ultrafast time scale, resulting in an electron transport of only a fraction of one nanometer. Following the relaxation of the initially injected momentum, backward motion of the electrons for about 1 ps is observed, driven by the Coulomb force from the oppositely moved holes. We also show that the injected current can be controlled by the phase of the laser pulses. These results demonstrate a new platform to study ballistic transport of nonequilibrium carriers in transition metal dichalcogenides.

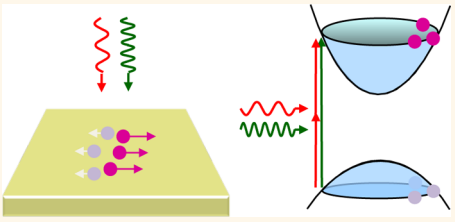

KEYWORDS: transition metal dichalcogenides · ReS_2 · ballistic · transport · coherent · control · quantum interference · charge transport

Recently, two-dimensional transitional metal dichalcogenides (TMDs), such as MoS_2 and WS_2, have drawn considerable attention as a new class of nanomaterials.[1] They have several exotic properties, including transition to a direct band gap in monolayers[2,3] and valley-selective optical coupling.[4−6] The in-plane charge transport is an important process that plays key roles in many potential applications of these materials, such as field-effect transistors,[7] solar cells,[8,9] and photodetectors.[9] Since 2010, significant progress has been made in understanding charge transport properties of various TMDs, through extensive investigations by many groups.[10−26] These studies have focused on one transport regime, drift-diffusion, with emphases on determining and improving the charge mobilities. The drift-diffusive transport is carried by equilibrium carriers with a well-defined energy distribution. Since multiple carrier scattering events are necessary for a carrier system to reach equilibrium energy and momentum distributions, drift-diffusive transport is established on a length scale longer than the mean free path of electrons, which is on the order of 10 to 100 nm under typical conditions. However, the channel length of semiconductor devices has been reduced to several tens of nanometers, which is comparable to the mean free path. In these nanoscale devices, ballistic transport of nonequilibium carriers with few or even no scattering events dominates the device performance. In fact, superior performance of TMD devices in the ballistic regime has been predicted theoretically.[27−31] For example, top-gated MoS_2 transistors with gate lengths of 15 nm can operate in the ballistic regime, with an on-current as high as 1.6 mA/μm and an on/off ratio of 10^{10}.[27,28] However, no experiments have been performed on this transport regime.

Here we demonstrate all-optical injection, control, and detection of ballistic currents in TMDs. We use a pair of ultrafast laser pulses to excite ReS_2 thin film samples by interband one-photon and two-photon absorption. The quantum interference between the two transition pathways allows us to inject and control ballistic currents. The currents are detected by spatially resolving the nanoscale transport of electrons associated with the ballistic currents.

* Address correspondence to huizhao@ku.edu.

Received for review December 18, 2014 and accepted March 12, 2015.

Published online 10.1021/acsnano.5b01111

We choose ReS_2, a relatively less studied TMD, in our experiments for several considerations. First, unlike most TMDs, which crystallize in hexagonal phase, ReS_2 forms a stable distorted 1*T* structure with triclinic symmetry.[32,33] As a consequence, the interlayer coupling in ReS_2 is much weaker than other TMDs,[32] with the adjacent monolayers largely decoupled. Hence, a multilayer ReS_2 behaves like a collection of noninteracting monolayers.[32] This allows us to study multilayer thin film samples, which yield larger signals and still reveal ballistic transport properties of monolayers. Second, the exciton binding energy in ReS_2 is about 20−30 meV,[34−36] much smaller than other TMDs.[37−39] This facilitates free carrier transport. Third, due to the unique lattice structure, ReS_2 possesses different properties from other TMDs, such as in-plane anisotropic optical responses.[40,41] Hence, it can be used to complement other TMDs in various applications.

RESULTS AND DISCUSSION

High-quality bulk crystals of ReS_2 were purchased from 2D Semiconductors. Thin film samples are obtained by mechanically cleaving the crystal with an adhesive tape, followed by depositing the cleaved flakes from the tape to a Si substrate with a 270 nm oxide layer. Two relatively large and uniform samples are selected for the measurements. Their thicknesses are 15 and 18 nm, respectively, determined by atomic force microscopy measurements (see the Supporting Information). All the measurements are performed at ambient conditions. In each sample, the laser spots are located near the center of the flake to avoid any potential edge effects. Similar results are obtained in both samples. We present results from the 15 nm sample in the main text and provide data from the 18 nm sample in the Supporting Information.

In our experiment, we use a coherence control technique[42] to inject ballistic currents. This current-injection process has been demonstrated in conventional semiconductors, such as Si[43] and GaAs,[44] as well as nanomaterials of carbon nanotubes[45] and graphene.[46] As shown in Figure 1a, a ReS_2 thin film sample is simultaneously illuminated by two 100 fs laser pulses with central wavelengths of 1500 nm (ω) and 750 nm (2ω), respectively. With a photon energy (1.65 eV) higher than the band gap of ReS_2 (about 1.5 eV),[34−36] the 2ω pulse injects electrons and holes *via* one-photon interband absorption (green vertical arrow). Usually, the transition amplitude of this one-photon absorption process, $A_1(\vec{k})$, is an even function of $\vec{k}$, the wavevector of the electrons. Hence, along any direction, an equal number of eletrons are injected with opposite $\vec{k}$ values, resulting in no net current. The ω pulse has a photon energy lower than the band gap and can inject carriers only by two-photon absorption (red vertical arrows). Although the transition amplitude of this two-photon process, A_2, is approximately an odd

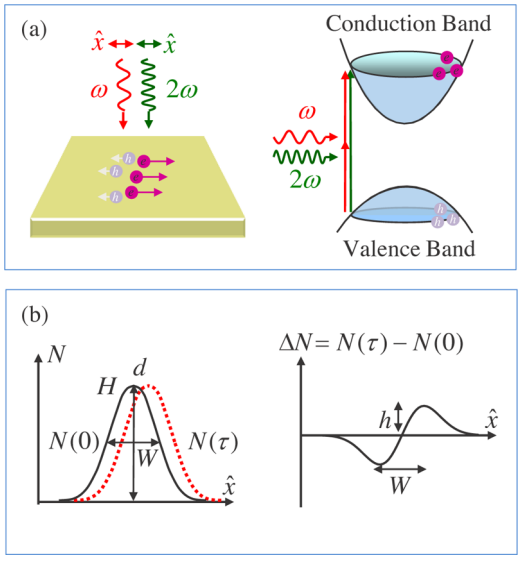

Figure 1. (a) Injection of ballistic currents by coherent control. The quantum interference between one-photon absorption of the 2ω pulse and two-photon absorption of the ω pulse allows control of the average velocities of the injected electrons and holes. (b) Differential pump−probe scheme to detect nanoscale transport. The initial electron density profile [*N*(0), solid Gaussian curve] and the profile at a later time [*N*(τ), dashed Gaussian curve] are separated by a small distance *d*. Their difference has a derivative-like profile (ΔN), with a height *h* that is proportional to *d*.

function of $\vec{k}$, the corresponding transition probability, $P_2 = |A_2|^2$, is still an even function of $\vec{k}$. Such a $\vec{k}$-space symmetry can be broken by utilizing the quantum interference effect: When the two transition pathways are present simultaneously, the overall transition probability is

$$P = |A_1 + A_2|^2 = |A_1|^2 + |A_2|^2 + A_1A_2^* + A_1^*A_2 \quad (1)$$

The last two terms on the right-hand side are the interference terms and are odd functions of $\vec{k}$. Therefore, in most cases, $P(k) \neq P(-k)$, making coherent control of current injection possible.[42] Specifically, when both pulses are linearly polarized along the same direction, defined as $\hat{x}$, electrons are injected in the conduction band with an average velocity of

$$\vec{v}_{av} = \eta v \sin(\Delta\phi)\hat{x} \quad (2)$$

where *v* is the speed of each electron determined by the excitation excess energy and $\Delta\phi = \phi_{2\omega} - 2\phi_\omega$ is the relative phase of the two transition amplitudes.[42] η is a parameter describing the efficiency of the current-injection process. Owing to the crystal momentum conservation, holes are injected in the valence band with an opposite crystal momentum. Once injected, the electrons and hole move oppositely along $\hat{x}$. Without a driving force, this ballistic current is expected to decay quickly, due to the phonon and carrier scattering. In addition, the Coulomb force also decelerates the electrons and the holes and eventually pulls them back toward the origin.

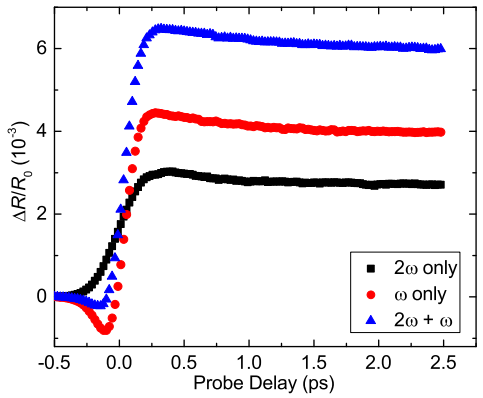

Figure 2. Differential reflection of the 810 nm probe pulse induced by the 2ω pump only (black squares), the ω pump only (red circles), and both pumps (blue triangles).

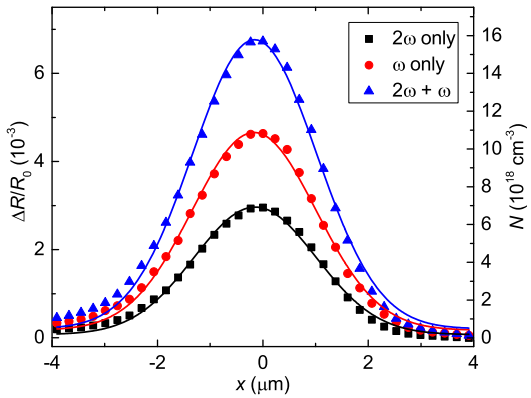

Figure 3. Spatial profiles of the carrier densities (right axis) injected by the 2ω (black squares), ω (red circles), and both (blue triangles) pump pules, estimated from the measured differential reflection (left axis) as the probe spot is scanned along $\hat{x}$ with a fixed probe delay of 0.35 ps. Here x = 0 is defined as where the centers of the pump and probe spots overlap.

We detect the injected carriers and currents by measuring differential reflection of a 100 fs and 810 nm probe pulse, $\Delta R/R_0 \equiv (R - R_0)/R_0$, where R and R_0 are the probe reflectance with the presence of the pump and without it, respectively. The black squares in Figure 2 show the measured $\Delta R/R_0$ with the 2ω pulse acting alone. The $\Delta R/R_0$ reaches a peak rapidly, limited by the time resolution of our system, and then decays relatively slowly. By using an absorption coefficient of 10^7 m^{-1} at 750 nm,[34] we estimate that the 2ω pulse with a peak energy fluence of 18 μJ cm^{-2} injects a carrier density of about 7 $\times$ 10^{18} cm^{-3} at the sample surface. We confirm that at this density level the $\Delta R/R_0$ signal is approximately proportional to the carrier density. This allows us to convert the measured $\Delta R/R_0$ to the carrier density. The $\Delta R/R_0$ signal measured with the ω pulse acting alone, with a fluence of 2 mJ cm^{-2}, is plotted as the red circles. On the basis of the magnitude of the signal, we estimate an injected carrier density of about 10^{19} cm^{-3}. We note that under this excitation condition no sample degradation was observed over the period of the whole study. An additional negative component can be seen around zero probe delays. This can be attributed to the nonlinear mixing of the probe and the ω pulses in the sample when they overlap, considering the rather high fluence of ω. This component does not influence our measurement at positive delays. The blue triangles in Figure 2 show the $\Delta R/R_0$ with both ω and 2ω pump pulses simultaneously present. It is slightly smaller than the sum of two other signals, which can be attributed to the saturation of the $\Delta R/R_0$ at high carrier densities.

Figure 3 shows the spatial profiles of $\Delta R/R_0$ excited by the 2ω (black squares), ω (red circles), and both (blue triangles) pumps, measured by scanning the probe spot along $\hat{x}$ with a fixed probe delay of 0.35 ps. The profiles can be fit well with Gaussian functions (solid curves), with a width (full width at half-maximum) of W = 2.8 μm. This width is consistent with the sizes of the laser spots of 2ω and ω and probe of 2, 3, and 2 μm, respectively. From the measured $\Delta R/R_0$, we estimate the injected carrier densities, as labeled on the right axis for convenience. As shown in Figure 1a, with both pumps present simultaneously, a ballistic current is injected, which causes the profile to move along $\hat{x}$. Hence, the center of the profile injected by the two pumps should be shifted with respect to the other two profiles. However, since the expected movement is much smaller than the size of the profile, which defines the spatial resolution of the measurement, it is not feasible to observe the transport by directly comparing these profiles.

In order to measure the nanoscale transport associated with the ballistic current, we use a differential pump−probe scheme that has been previously used to study ballistic transport in conventional semiconductors such as GaAs, Si, and Ge.[47−49] As illustrated in Figure 1b, the two pump pulses inject electrons to the conduction band, with a Gaussian spatial profile shown as the black solid curve [N(0), with a height H and a width W]. By choosing $\Delta\phi = \pi/2$, these electrons are injected with an average velocity along $+\hat{x}$ (eq 2). After a short period of time (τ), the profile moves by a distance of d [red dotted Gaussian curve, $N(\tau)$], where $d \ll W$. To deduce d, we directly measure the difference between the final and initial profiles, $\Delta N = N(\tau) - N(0)$. It has a derivative-like spatial profile with the positive and negative extremes separated by W (Figure 1d). It can be viewed as the change of the electron density, or electron accumulation, due to the transport. The amplitude of this profile, h, is proportional to d. In fact, it is straightforward to show that

$$\frac{d}{W} = 0.707\frac{h}{H} \qquad (3)$$

Hence, by measuring H, W, and h, we can deduce d even though it is several orders of magnitude smaller than the laser spots. The measurements of H and W are shown in Figure 3. The measurement of h, the

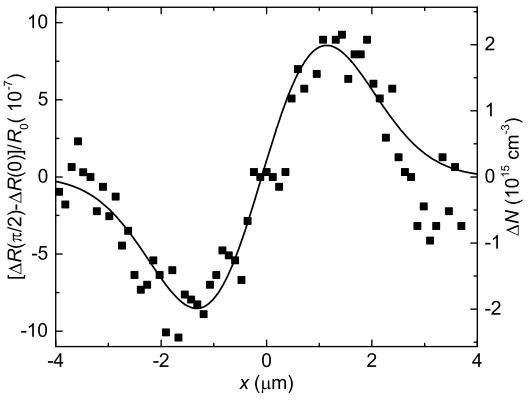

Figure 4. Transport-induced electron accumulation (right axis) deduced from the measured difference between the differential reflection signals with $\Delta\phi = \pi/2$ and $\Delta\phi = 0$ (left axis). The probe delay is 0.35 ps.

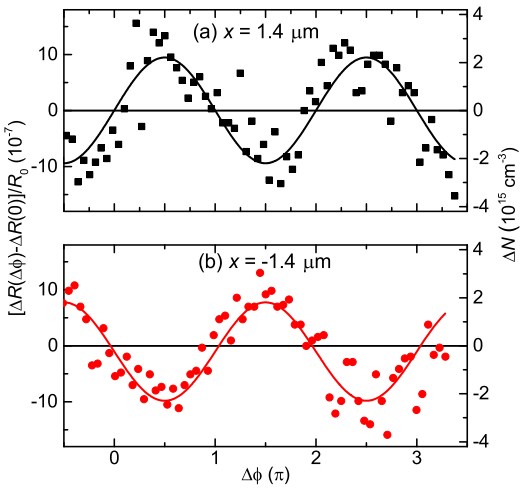

Figure 5. Electron accumulation due to transport as a function of $\Delta\phi$ measured at probe positions of 1.4 μm (a) and -1.4 μm (b), respectively. The probe delay is 0.35 ps.

magnitude of ΔN, is achieved by modulating the $\Delta\phi$ between $\pi/2$ and 0. With $\Delta\phi = 0$, no current is injected, and the profile stays at its initial position [$N(0)$]. Hence, the different between the two profiles at τ with $\Delta\phi = \pi/2$ and 0, respectively, equals ΔN.

Figure 4 shows the measured differential pump–probe signal, $[\Delta R(\Delta\phi = \pi/2) - \Delta R(\Delta\phi = 0)]/R_0$, with the probe delay of 0.35 ps. By using the established relation between $\Delta R/R_0$ and N, we deduce ΔN from this signal, as labeled on the right axis. Clearly, ΔN has a derivative-like profile, as confirmed by a fit (solid line). From the magnitude of $h \approx 2 \times 10^{15}$ cm^{-3}, and by using $H \approx 1.6 \times 10^{19}$ cm^{-3} and $W \approx 2.8$ μm (Figure 3), we estimated a transport distance of about 0.3 nm (eq 3). We note that although the process of deducing the ΔN and N individually from the measured differential reflection relies on knowledge of the absorption coefficient and pump fluence and is subject to the influence of saturation, only the ratio $\Delta N/N$ is used in obtaining the transport length. This ratio is not influenced by any of these factors.

In the optically injected ballistic currents, the electrons and the holes move oppositely since they have opposite crystal momenta. The signal plotted in Figure 4 mainly originates from the electrons since the electron effective mass is a few times smaller than the holes, according to the calculated band structure of ReS_2.[32] With a smaller effective mass, the electrons are more efficient in inducing a transient absorption signal *via* phase-space state filling.[50] More importantly, electrons are injected with a higher average velocity and hence move a larger distance than the holes. On the basis of these two factors, we attribute the observed ΔN to the electron density, and the transport length to be the electron transport length.

To demonstrate coherent control of the injected ballistic current, we measure ΔN as a function of $\Delta\phi$ at a probe delay of 0.35 ps and a probe position of $x = 1.4$ μm. This is achieved by measuring the quantity $[\Delta R(\Delta\phi) - \Delta R(\Delta\phi = 0)]/R_0$, as $\Delta\phi$ is varied.

The results plotted in Figure 5a show a clear sinusoidal dependence, as confirmed by a fit (solid line). When the probe spot is moved to $x = -1.4$ μm, the signal changes sign, as shown in Figure 5b. This is consistent with the fact that accumulation of electrons on one side of the profile, due to the transport, is always accompanied by a depletion on the other side, as illustrated in Figure 4. Since ΔN (and d) is proportional to the initial velocity of electrons and the thus the injected current density, this measurement demonstrates the phase control of the current injection process.

These measurements performed at a fixed probe delay of 0.35 ps demonstrate optical injection and coherent control of ballistic currents in ReS_2. To reveal the dynamics of the injected ballistic currents, we attempt to time resolve the transport process. The measurement is performed by repeating the scan shown in Figure 5a at various probe delays. The deduced d as a function of probe delay is shown in Figure 6. Despite the rather large error bars due to the laser intensity noise, we can draw a few conclusions. First, the transport distance reaches a peak right after zero probe delay. This indicates that the velocity of the electrons in the injected ballistic currents drops to zero within our time resolution of about 200 fs. Both phonon scattering and electron–hole scattering can contribute to such a fast momentum relaxation process. Considering the high carrier density used in this experiment, we expect the latter to make a bigger contribution. Second, the d decreases to about 20% of its peak value in about 1 ps. This indicates that once the electrons reach their maximal displacement, the Coulomb force from the oppositely moving holes pull them back toward their original position. Third, the d maintains a value slightly larger than zero for the rest of the time, indicating the electrons do not return to their original position. Since the electrons can rest only when they overlap with the holes, this nonzero final transport length indicates that

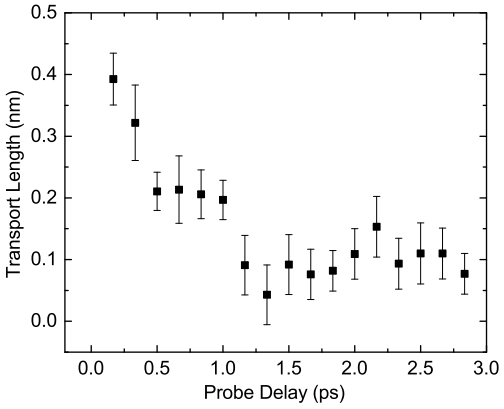

Figure 6. Time evolution of the transport length of electrons.

there is a small center-of-mass motion of the electron–hole system. Since the electron–hole system in the injected ballistic current has no net crystal momentum, such a center-of-mass motion indicates that the carrier system has gained momentum from the lattice during the transport. This can occur because electrons and holes both interact with phonons during their transport and transfer part of their momenta to phonons. Since they have different effective masses and densities of state, their phonon scattering rates are expected to be different. This imbalance of momentum relaxation of electrons and holes due to phonon scattering causes a nonzero net momentum of the electron–hole system and a center-of-mass movement. In addition, traps that capture electrons and holes during their transport can also contribute to the observed nonzero final displacement. However, given the short transport time of just 1 ps, we expect this process to play a minor role.

Finally, we note that these measurements are performed with fixed energy fluences of ω and 2ω pulses. No attempts are made to study the dependence of the current-injection efficiency on the pump fluence for two reasons: First, the single-to-noise ratio does not allow us to reduce the pump fluence over a large range. Second, even if one could measure the transport length at different pump fluences, such a dependence does not directly reflect the current-injection efficiency since the decay of the current also depends on the pump fluence.

CONCLUSION

We demonstrated all-optical injection, control, and detection of ballistic currents in ReS_2, a transition metal dichalcogenide. By utilizing quantum interference between one-photon and two-photon interband transition pathways, we injected ballistic currents in ReS_2 thin film samples by using a pair of ultrafast laser pulses. The currents are detected by spatially resolving the nanoscale transport of electrons over a distance of only a fraction of one nanometer. We show that the injected current density can be coherently controlled by the phase of the laser pulses. Furthermore, by time resolving the current dynamics, we found that the current decays on a ultrafast time scale, due to the strong scattering. We also observed the backward motion of electrons for about 1 ps after the relaxation of their initially injected velocity, driven by the Coulomb force from the oppositely moved holes. These results demonstrate a new platform to study ballistic transport of nonequilibrium carriers in TMDs.

METHODS

In the experimental setup, the 532 nm output of a diode laser is used to pump a Ti:sapphire laser, which generates 100 fs pulses with a central wavelength of 810 nm at about 81 MHz. A beamsplitter is used to reflect 8% of this pulse, which is used as the probe. The majority of the 810 nm pulse is used to pump an optical parametric oscillator, which generates a signal output with a central wavelength of 1500 nm. By focusing the 1500 nm pulse to a beta barium borate crystal, we generate its second harmonic at 750 nm. A dichroic beamsplitter separates the 1500 and 750 nm pulses, used as the ω and 2ω pulses, respectively. Each pulse goes through a half-wave plate and a polarizer to control the polarization and the power. Another dichroic beamsplitter is used to combine the two pulses, which are focused to the sample by using a microscope objective lens. An electrooptical phase modulator is used in the 2ω arm to modulate its phase. A piezoelectric translation stage is used in the ω arm to vary the phase of the ω pulse. Hence, the relative phase of the two pulses can be independently modulated and varied with a high precision. These phase control procedures are calibrated by observing second-harmonic generation of the ω pulse in a GaAs crystal with the presence of the 2ω pulse.

To probe the carriers and the currents injected by the ω and 2ω pulses, the 810 pulse is focused to the sample through the same objective lens. The reflected probe is sent to one silicon photodetector as a part of a balanced detector. Before entering the objective lens, a portion of the 810 nm pulse is sent to the other photodetector of the balanced detector as a reference, which power matches the power of the reflected probe with the pump beam blocked. By using this balanced detector scheme, the intensity noise of the 810 nm beam is equally distributed to the probe and the reference beams and is therefore significantly suppressed at the output of the balanced detector (which substracts the reference from the probe). To further reduce the noise, the output of the balanced detector is measured with a lock-in amplifier. When probing the carriers, the intensity of the pump beams is modulated at about 2 kHz. When measuring the transport-induced electron accumulation, the relative phase of the two pump pulses is modulated at about 2.5 kHz.

Conflict of Interest: The authors declare no competing financial interest.

Acknowledgment. The authors thank Jamie Wilt and Judy Wu for their help on AFM measurements. This material is based upon work supported by the National Science Foundation (USA) under Award Nos. DMR-0954486 and IIA-1430493.

Supporting Information Available: Sample fabrication and characterization; estimation of carrier density; carrier lifetime; results of another sample. This material is available free of charge *via* the Internet at http://pubs.acs.org.

REFERENCES AND NOTES

1. Wang, Q. H.; Kalantar-Zadeh, K.; Kis, A.; Coleman, J. N.; Strano, M. S. Electronics and Optoelectronics of Two-Dimensional Transition Metal Dichalcogenides. *Nat. Nanotechnol.* **2012**, *7*, 699–712.
2. Mak, K. F.; Lee, C.; Hone, J.; Shan, J.; Heinz, T. F. Atomically Thin MoS_2: A New Direct-Gap Semiconductor. *Phys. Rev. Lett.* **2010**, *105*, 136805.
3. Splendiani, A.; Sun, L.; Zhang, Y.; Li, T.; Kim, J.; Chim, C. Y.; Galli, G.; Wang, F. Emerging Photoluminescence in Monolayer MoS_2. *Nano Lett.* **2010**, *10*, 1271–1275.
4. Xiao, D.; Liu, G. B.; Feng, W.; Xu, X.; Yao, W. Coupled Spin and Valley Physics in Monolayers of MoS_2 and Other Group-VI Dichalcogenides. *Phys. Rev. Lett.* **2012**, *108*, 196802.
5. Zeng, H.; Dai, J.; Yao, W.; Xiao, D.; Cui, X. Valley Polarization in MoS_2 Monolayers by Optical Pumping. *Nat. Nanotechnol.* **2012**, *7*, 490–493.
6. Mak, K. F.; He, K.; Shan, J.; Heinz, T. F. Control of Valley Polarization in Monolayer MoS_2 by Optical Helicity. *Nat. Nanotechnol.* **2012**, *7*, 494–498.
7. Radisavljevic, B.; Radenovic, A.; Brivio, J.; Giacometti, V.; Kis, A. Single-Layer MoS_2 Transistors. *Nat. Nanotechnol.* **2011**, *6*, 147–150.
8. Pospischil, A.; Furchi, M. M.; Mueller, T. Solar-Energy Conversion and Light Emission in an Atomic Monolayer P-N Diode. *Nat. Nanotechnol.* **2014**, *9*, 257–261.
9. Baugher, B. W. H.; Churchill, H. O. H.; Yang, Y.; Jarillo-Herrero, P. Optoelectronic Devices Based on Electrically Tunable P-N Diodes in a Monolayer Dichalcogenide. *Nat. Nanotechnol.* **2014**, *9*, 262–267.
10. Zhang, Y.; Ye, J.; Matsuhashi, Y.; Iwasa, Y. Ambipolar MoS_2 Thin Flake Transistors. *Nano Lett.* **2012**, *12*, 1136–1140.
11. Pu, J.; Yomogida, Y.; Liu, K. K.; Li, L. J.; Iwasa, Y.; Takenobu, T. Highly Flexible MoS_2 Thin-Film Transistors with Ion Gel Dielectrics. *Nano Lett.* **2012**, *12*, 4013–4017.
12. Chen, J. R.; Odenthal, P. M.; Swartz, A. G.; Floyd, G. C.; Wen, H.; Luo, K. Y.; Kawakami, R. K. Control of Schottky Barriers in Single Layer MoS_2 Transistors with Ferromagnetic Contacts. *Nano Lett.* **2013**, *13*, 3106–3110.
13. Das, S.; Chen, H. Y.; Penumatcha, A. V.; Appenzeller, J. High Performance Multilayer MoS_2 Transistors with Scandium Contacts. *Nano Lett.* **2013**, *13*, 100–105.
14. Liu, W.; Kang, J. H.; Sarkar, D.; Khatami, Y.; Jena, D.; Banerjee, K. Role of Metal Contacts in Designing High-Performance Monolayer N-Type WSe_2 Field Effect Transistors. *Nano Lett.* **2013**, *13*, 1983–1990.
15. Zhang, Y. J.; Ye, J. T.; Yornogida, Y.; Takenobu, T.; Iwasa, Y. Formation of a Stable P-N Junction in a Liquid-Gated MoS_2 Ambipolar Transistor. *Nano Lett.* **2013**, *13*, 3023–3028.
16. Das, S.; Appenzeller, J. Where Does the Current Flow in Two-Dimensional Layered Systems? *Nano Lett.* **2013**, *13*, 3396–3402.
17. Radisavljevic, B.; Kis, A. Mobility Engineering and a Metal-Insulator Transition in Monolayer MoS_2. *Nat. Mater.* **2013**, *12*, 815–820.
18. Qiu, H.; Xu, T.; Wang, Z.; Ren, W.; Nan, H.; Ni, Z.; Chen, Q.; Yuan, S.; Miao, F.; Song, F.; *et al*. Hopping Transport through Defect-Induced Localized States in Molybdenum Disulphide. *Nat. Commun.* **2013**, *4*, 2642.
19. Radisavljevic, B.; Whitwick, M. B.; Kis, A. Integrated Circuits and Logic Operations Based on Single-Layer MoS_2. *ACS Nano* **2011**, *5*, 9934–9938.
20. Wang, H.; Yu, L. L.; Lee, Y. H.; Shi, Y. M.; Hsu, A.; Chin, M. L.; Li, L. J.; Dubey, M.; Kong, J.; Palacios, T. Integrated Circuits Based on Bilayer MoS_2 Transistors. *Nano Lett.* **2012**, *12*, 4674–4680.
21. Zhu, W. J.; Low, T.; Lee, Y. H.; Wang, H.; Farmer, D. B.; Kong, J.; Xia, F. N.; Avouris, P. Electronic Transport and Device Prospects of Monolayer Molybdenum Disulphide Grown by Chemical Vapour Deposition. *Nat. Commun.* **2014**, *5*, 3087.
22. Radisavljevic, B.; Kis, A. Measurement of Mobility in Dual-Gated MoS_2 Transistors. *Nat. Nanotechnol.* **2013**, *8*, 147–148.
23. Chamlagain, B.; Li, Q.; Ghimire, N. J.; Chuang, H. J.; Perera, M. M.; Tu, H.; Xu, Y.; Pan, M.; Xiao, D.; Yan, J.; *et al*. Mobility Improvement and Temperature Dependence in $MoSe_2$ Field-Effect Transistors on Parylene-C Substrate. *ACS Nano* **2014**, *8*, 5079–5088.
24. Pradhan, N. R.; Rhodes, D.; Xin, Y.; Memaran, S.; Bhaskaran, L.; Siddiq, M.; Hill, S.; Ajayan, P. M.; Balicas, L. Ambipolar Molybdenum Diselenide Field-Effect Transistors: Field-Effect and Hall Mobilities. *ACS Nano* **2014**, *8*, 7923–7929.
25. Ovchinnikov, D.; Allain, A.; Huang, Y. S.; Dumcenco, D.; Kis, A. Electrical Transport Properties of Single-Layer WS_2. *ACS Nano* **2014**, *8*, 8174–8181.
26. Allain, A.; Kis, A. Electron and Hole Mobilities in Single-Layer WSe_2. *ACS Nano* **2014**, *8*, 7180–7185.
27. Liu, L.; Kumar, S. B.; Ouyang, Y.; Guo, J. Performance Limits of Monolayer Transition Metal Dichalcogenide Transistors. *IEEE Trans. Elec. Dev.* **2011**, *58*, 3042–3047.
28. Yoon, Y.; Ganapathi, K.; Salahuddin, S. How Good Can Monolayer MoS_2 Transistors Be. *Nano Lett.* **2011**, *11*, 3768–3773.
29. Sengupta, A.; Ghosh, R. K.; Mahapatra, S. Performance Analysis of Strained Monolayer MoS_2 MOSFET. *IEEE Trans. Electron Devices* **2013**, *60*, 2782–2787.
30. Kormanyos, A.; Zolyomi, V.; Drummond, N. D.; Rakyta, P.; Burkard, G.; Fal'ko, V. I. Monolayer MoS_2: Trigonal Warping, the Gamma Valley, and Spin-Orbit Coupling Effects. *Phys. Rev. B* **2013**, *88*, 045416.
31. Chang, J. W.; Register, L. F.; Banerjee, S. K. Ballistic Performance Comparison of Monolayer Transition Metal Dichalcogenide MX_2 (M = Mo, W; X = S, Se, Te)Metal-Oxide-Semiconductor Field Effect Transistors. *J. Appl. Phys.* **2014**, *115*, 084506.
32. Tongay, S.; Sahin, H.; Ko, C.; Luce, A.; Fan, W.; Liu, K.; Zhou, J.; Huang, Y.-S.; Ho, C.-H.; Yan, J.; *et al*. Monolayer Behaviour in Bulk ReS_2 Due to Electronic and Vibrational Decoupling. *Nat. Commun.* **2014**, *5*, 3252.
33. Kelty, S. P.; Ruppert, A. F.; Chianelli, R. R.; Ren, J.; Whangbo, M. H. Scanning Probe Microscopy Study of Layered Dichalcogenide ReS_2. *J. Am. Chem. Soc.* **1994**, *116*, 7857–7863.
34. Friemelt, K.; Kulikova, L.; Kulyuk, L.; Siminel, A.; Arushanov, E.; Kloc, C.; Bucher, E. Optical and Photoelectrical Properties of ReS_2 Single Crystals. *J. Appl. Phys.* **1996**, *79*, 9268–9272.
35. Ho, C. H.; Liao, P. C.; Huang, Y. S.; Tiong, K. K. Temperature Dependence of Energies and Broadening Parameters of the Band-Edge Excitons of ReS_2 and $ReSe_2$. *Phys. Rev. B* **1997**, *55*, 15608–15613.
36. Ho, C. H.; Huang, Y. S.; Chen, J. L.; Dann, T. E.; Tiong, K. K. Electronic Structure of ReS_2 and $ReSe_2$ from First-Principles Calculations, Photoelectron Spectroscopy, and Electrolyte Electroreflectance. *Phys. Rev. B* **1999**, *60*, 15766–15771.
37. Chernikov, A.; Berkelbach, T. C.; Hill, H. M.; Rigosi, A.; Li, Y. L.; Aslan, O. B.; Reichman, D. R.; Hybertsen, M. S.; Heinz, T. F. Exciton Binding Energy and Nonhydrogenic Rydberg Series in Monolayer WS_2. *Phys. Rev. Lett.* **2014**, *113*, 076802.
38. He, K.; Kumar, N.; Zhao, L.; Wang, Z.; Mak, K. F.; Zhao, H.; Shan, J. Tightly Bound Excitons in Monolayer WSe_2. *Phys. Rev. Lett.* **2014**, *113*, 026803.
39. Ye, Z.; Cao, T.; O'Brien, K.; Zhu, H.; Yin, X.; Wang, Y.; Louie, S. G.; Zhang, X. Probing Excitonic Dark States in Single-Layer Tungsten Disulphide. *Nature* **2014**, *513*, 214–218.
40. Friemelt, K.; Luxsteiner, M. C.; Bucher, E. Optical-Properties of the Layered Transition-Metal-Dichalcogenide ReS_2 - Anisotropy in the Van-Der-Waals Plane. *J. Appl. Phys.* **1993**, *74*, 5266–5268.
41. Ho, C. H.; Huang, Y. S.; Tiong, K. K.; Liao, P. C. Absorption-Edge Anisotropy in ReS_2 and $ReSe_2$ Layered Semiconductors. *Phys. Rev. B* **1998**, *58*, 16130–16135.
42. Atanasov, R.; Haché, A.; Hughes, J. L. P.; van Driel, H. M.; Sipe, J. E. Coherent Control of Photocurrent Generation in Bulk Semiconductors. *Phys. Rev. Lett.* **1996**, *76*, 1703–1706.
43. Costa, L.; Betz, M.; Spasenovic, M.; Bristow, A. D.; van Driel, H. M. All-Optical Injection of Ballistic Electrical Currents in Unbiased Silicon. *Nat. Phys.* **2007**, *3*, 632–635.

44. Haché, A.; Kostoulas, Y.; Atanasov, R.; Hughes, J. L. P.; Sipe, J. E.; van Driel, H. M. Observation of Coherently Controlled Photocurrent in Unbiased, Bulk GaAs. *Phys. Rev. Lett.* **1997**, *78*, 306.
45. Newson, R. W.; Menard, J. M.; Sames, C.; Betz, M.; van Driel, H. M. Coherently Controlled Ballistic Charge Currents Injected in Single-Walled Carbon Nanotubes and Graphite. *Nano Lett.* **2008**, *8*, 1586–1589.
46. Sun, D.; Divin, C.; Rioux, J.; Sipe, J. E.; Berger, C.; de Heer, W. A.; First, P. N.; Norris, T. B. Coherent Control of Ballistic Photocurrents in Multilayer Epitaxial Graphene Using Quantum Interference. *Nano Lett.* **2010**, *10*, 1293–1296.
47. Werake, L. K.; Ruzicka, B. A.; Zhao, H. Observation of Intrinsic Inverse Spin Hall Effect. *Phys. Rev. Lett.* **2011**, *106*, 107205.
48. Zhao, H.; Smirl, A. L. Injection and Detection of Ballistic Electrical Currents in Silicon. *Appl. Phys. Lett.* **2010**, *97*, 212106.
49. Loren, E. J.; Ruzicka, B. A.; Werake, L. K.; Zhao, H.; van Driel, H. M.; Smirl, A. L. Optical Injection and Detection of Ballistic Pure Spin Currents in Ge. *Appl. Phys. Lett.* **2009**, *95*, 092107.
50. Schmitt-Rink, S.; Chemla, D. S.; Miller, D. A. B. Theory of Transient Excitonic Optical Nonlinearities in Semiconductor Quantum-Well Structures. *Phys. Rev. B* **1985**, *32*, 6601–6609.